An AI Based Algorithm for Retrieving Aerosol Optical Depth and Single Scattering Albedo Using All-Sky Imager Observations

Heyang Ni[1], Jing Li[*,1,2,3], Liang Chang[1], Yueming Dong[1], Guanghao Du[1], Muqian Li[1], Qiurui Li[1], Guanyu Liu[1], Yuebo Sun[1], Angnuo Tian[1], Sheng Yue[1], Chongzhao Zhang[1], Zhenyu Zhang[1]

[1]Department of Atmospheric and Oceanic Sciences, School of Physics, Peking University, Beijing, China
[2]Institute of Carbon Neutrality, Peking University, Beijing, China
[3]Center for Environment and Health, Peking University, Beijing, China

Correspondence to: jing-li@pku.edu.cn

Abstract. Accurate measurement of aerosol optical properties is critical for understanding their radiative and environmental impacts. Currently, the most accurate retrieval of aerosol properties comes from the multi-channel surface sun photometer, but with relatively high cost and deployment/maintenance requirements. Here we develop a novel AI based method for retrieving daytime aerosol optical parameters, namely aerosol optical depth (AOD) and single scattering albedo (SSA) using images acquired by All-Sky Imagers (ASI). Surface based AOD and SSA retrievals from surface sun photometers are used as the training targets. Algorithm training and retrievals were performed for two sites in East China and Central US respectively. Independent validation against ground-based measurements demonstrated high consistency between the ASI-retrieved and sun photometer measured AOD and SSA, with Pearson correlation coefficients (r) exceeding 0.86 for AOD across all wavelengths at both sites and Root Mean Square Errors (RMSE) below 0.25. For SSA, r values reached 0.74 at the Beijing_PKU site and 0.84 at the SGP site, with RMSE remaining below 0.09 across all spectral channels, demonstrating the feasibility of simultaneous AOD and SSA retrieval from low-cost all-sky imagers. These results demonstrate the feasibility of simultaneous AOD and SSA retrieval from ASI imagery and suggest that low-cost sky cameras may become a useful complement to sun-photometer networks after broader validation across additional environments, seasons, instruments, and aerosol types.

1 Introduction

Aerosol radiative forcing remains a major source of uncertainty in climate assessment due to its high spatiotemporal heterogeneity and complex composition (Bellouin et al., 2020; Boucher et al., 2013; Intergovernmental Panel On Climate Change (Ipcc), 2023; Li et al., 2017). Mitigating this requires accurate retrieval of optical properties, particularly Aerosol Optical Depth (AOD) and Single Scattering Albedo (SSA) (Hansen et al., 1997; Hao et al., 2024; Levy et al., 2013). While ground-based sun photometers, such as those used within the Aerosol Robotic Network (AERONET) can provide the most accurate retrievals of aerosol properties (Holben et al., 1998), the relatively high cost of the instrument limits their extensive spatial deployments.

Traditional aerosol monitoring networks, such as AERONET, provide high accuracy but are limited by high equipment costs and sparse spatial coverage. To address this, various low-cost retrieval methods have been developed (Kazantzidis et al., 2017; Snik et al., 2014). These include retrieving AOD from long-term visibility records(Hao et al., 2024), employing all-sky imaging systems combined with machine learning (Scarlatti et al., 2023), and utilizing portable handheld sun-photometers like Calitoo (García et al., 2025). Among them, the all-sky imager (ASI), originally designed for automated ground-based cloud cover monitoring to replace manual observations, has emerged as a powerful tool for environmental research (Sabburg and Wong, 1999). Typically equipped with a fisheye lens and Charge-Coupled Device (CCD) sensors, these cameras capture high spatial-and-temporal-resolution visible-light images across the entire sky dome. Recent advancements in quality and calibration have rendered ASIs highly suitable for atmospheric measurement (Ghonima et al., 2012; Kazantzidis et al., 2012, 2017; Tohsing et al., 2013; Valdelomar et al., 2021). Numerous studies have demonstrated the potential of All-Sky Imagers (ASIs) for retrieving aerosol optical properties. Early approaches primarily relied on Radiative Transfer Models (RTM) and Look-Up Tables (LUTs) to link sky radiance or the Red-to-Blue Ratio (RBR) to AOD (Huo and Lü, 2010; Olmo et al., 2008). With the advent of data-driven techniques, Machine Learning (ML) and Deep Learning models have been increasingly applied, utilizing pixel-level features and circumsolar information to bypass complex physical calibrations (Logothetis et al., 2023; Scarlatti et al., 2023).

Compared to traditional sun photometers, ASIs offer three significant advantages: lower equipment and maintenance costs; enhanced spatial coverage, particularly in remote areas like deserts or solar power plants where stations are sparse (Kazantzidis et al., 2017); and the avoidance of temporal delays, as ASIs capture radiance from multiple sky locations simultaneously rather than sequentially (Román et al., 2022). However, quantitative inversion of aerosol properties from ASI data faces significant challenges. Historically, ASI-based aerosol retrievals have predominantly relied on extracting sky radiances or RGB channel intensities and mapping them to Aerosol Optical Depth (AOD) (Rossini and Krenzinger, 2007; Tohsing et al., 2013). These inversions are typically driven either by establishing a lookup table (LUT) between the radiation ratio (blue/red light) and AOD (Huo and Lü, 2010), or by employing data-driven machine learning algorithms (Cazorla et al., 2009; Logothetis et al., 2023; Scarlatti et al., 2023). While these pioneering studies have demonstrated reasonable AOD estimation accuracy—often achieving Root Mean Square Errors (RMSE) of less than 0.1 when validated against standard AERONET measurements under clear-sky conditions (Logothetis et al., 2023; Scarlatti et al., 2023)—their practical applications remain restricted. Most of these works are confined to single-station validations, leaving their multi-station scalability and robustness under varying surface albedos largely untested.

Furthermore, traditional inversion approaches are computationally complex and inefficient, typically involving resource-intensive iterative adjustments of inputs into RTMs (Olmo et al., 2008). Crucially, most existing ASI-based studies focus solely on AOD inversion. They fail to achieve the simultaneous retrieval of aerosol scattering properties, hindering an integrated analysis of aerosol mass and particle composition at fine scales.

The visible-band imagery captured by ASIs not only contains direct attenuation of solar radiation that is essential to derive AOD, but also captures characteristics of diffuse radiation, which is typically measured by sun photometers to retrieve SSA (Dubovik and King, 2000). However, this feature is not fully utilized by previous aerosol retrieval practices with ASI. To address this gap, this study proposes a scheme to simultaneously retrieve AOD and SSA from ASI images. By developing an eXtreme Gradient Boosting (XGBoost) regression model (Chen and Guestrin, 2016), we leverage the capability of these algorithms to uncover patterns within the data. This approach also greatly simplifies the complex iterative process of traditional inversion to enhance efficiency. Compared with previous ASI-based aerosol retrieval studies, the present method differs in four main aspects. First, previous studies generally used sky radiance, RGB intensity, red-to-blue ratio, or circumsolar features mainly for AOD retrieval, whereas this study uses multi-region RGB and geometric features from ASI images to retrieve both AOD and SSA. Second, the retrieval target is expanded from aerosol loading alone to both aerosol loading and aerosol absorption/scattering properties, which are represented by AOD and SSA, respectively. Third, the method is evaluated at two climatically different sites, Beijing_PKU and SGP, using collocated sun-photometer products as independent reference data, rather than being limited to a single-site demonstration. Finally, once the model is trained, the retrieval does not require iterative radiative transfer calculations or repeated LUT searches, making the method computationally efficient for high-temporal-resolution ASI observations. A concise comparison between the present method and representative previous ASI-based aerosol retrieval studies is provided in Table S1. Our algorithm provides a pathway for extensive low-cost aerosol observations, thus providing practical value for reducing aerosol-related uncertainties in climate assessments.

2. Data and Method

2.1 All-Sky Imager Data

The data used in this study were collected at two sites: Beijing in north China and the Southern Great Plain (SGP) site in central US. The ASI data in Beijing were collected by an SRF-02 All-Sky Imager manufactured by EKO. This imager lacks a solar occulting device, and representative clear-sky and cloudy-sky images from the Beijing_PKU ASI are shown in Fig. 1a and Fig. 1b, respectively. The all-sky imager was installed at the School of Physics, Peking University (39°59'N, 116°18'E). Images were captured between April 2017 and January 2020, with a resolution of 2272 × 1704 pixels at 180 dpi, totalling approximately 200,000 images.

Representative clear-sky and cloudy-sky images from the SGP TSI are shown in Fig. 1c and Fig. 1d, respectively. The SGP site, operated by the U.S. Department of Energy's Atmospheric Radiation Measurement (ARM) program, serves as a key atmospheric observation station (Cook and Sullivan, 2025; Stokes and Schwartz, 1994). Sky conditions were monitored using the Total Sky Imager (TSI), Model TSI-660, developed by Yankee Environmental Systems (YES), Inc. To evaluate the model's performance under different climatic conditions and geographical contexts, data spanning from January 2024 to November 2024 were selected from the SGP site. This period is distinct from the Beijing dataset (2018–2020), providing an opportunity to assess the method's transferability and robustness across different environments.

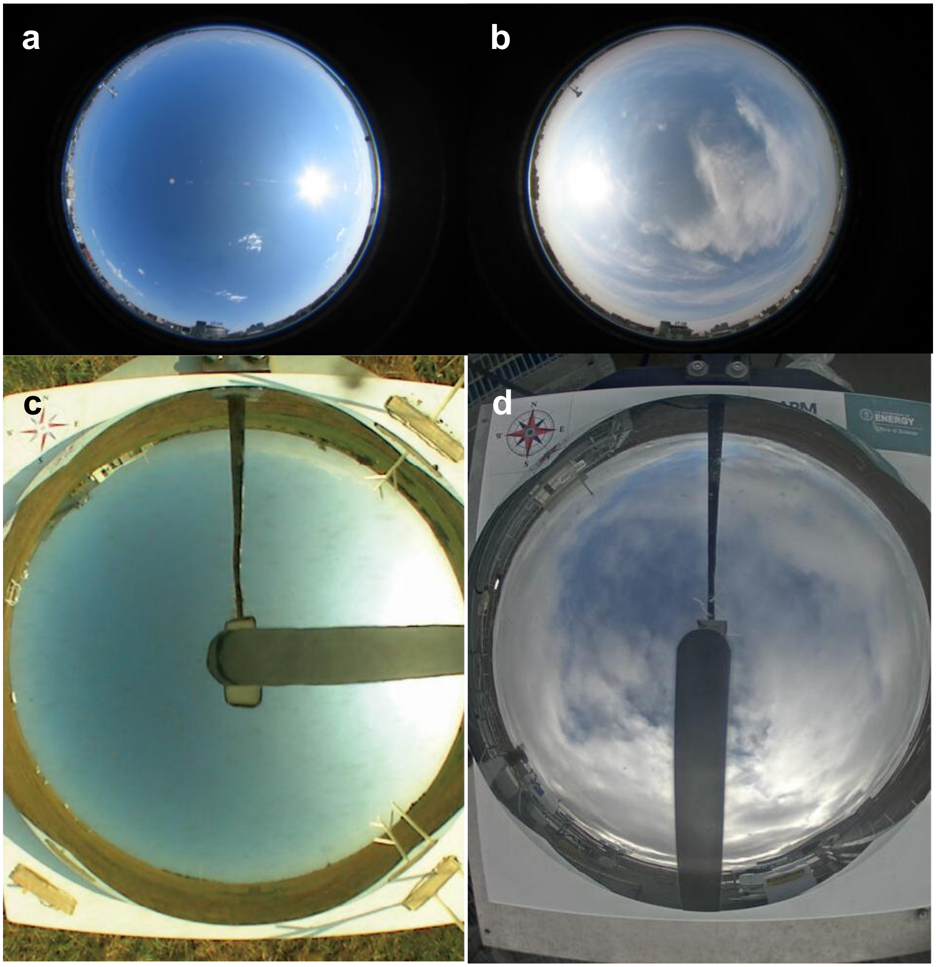

Figure 1: (a) A sample image captured by Beijing_PKU site ASI; (b) A sample cloud image captured by Beijing site ASI; (c) A sample image captured by SGP site ASI; (d) A sample cloud image captured by SGP site ASI. Source for (a, b): all-sky imager observations collected by the authors' research group at Beijing_PKU. Source for (c, d): ARM user facility (https://adc.arm.gov/discovery/results/instrument_class_code::tsi), licensed under CC BY 4.0 (https://creativecommons.org/licenses/by/4.0/). Last access: 21 April 2026.

2.2 Sun Photometer Data

The target AOD and SSA are obtained from collocated surface sun photometers, namely those at the ‘Beijing_PKU’ and ‘ARM_SGP’ sites of AERONET. AOD from direct measurements and SSA retrieved from diffuse sky measurements at four wavelengths (440, 675, 870, and 1020 nm) are used. The dataset covers the period from 2017 to 2021 for Beijing_PKU and from 2024 to 2025 for SGP. For the SGP site, we utilized the Version 3 Level 2.0 (cloud-screened and quality-assured) data products for both AOD and SSA. This dataset represents the highest quality standard of AERONET, providing a robust benchmark for model validation in cleaner atmospheric environments. For the Beijing_PKU site, AERONET Version 3 Level 2.0 SSA inversion products were not available during the period overlapping with the ASI observations, mainly because the post-deployment calibration required for Level 2.0 quality assurance could not be completed in time due to pandemic-related restrictions on international shipment and calibration. Therefore, Version 3 Level 1.5 inversion products were used as the reference targets for Beijing SSA retrieval. Although Level 1.5 products are cloud-screened, they have not undergone the full quality-assurance procedure applied to Level 2.0 products. To reduce the potential uncertainty associated with Level 1.5 SSA, we further applied additional quality-control criteria to the Beijing inversion records. Specifically, only SSA retrievals with solar zenith angle greater than 50° and sky residual less than 5% were retained. These criteria remove less stable sky-radiance inversion cases associated with unfavorable observation geometry or relatively large fitting residuals, for which SSA retrievals are expected to be more uncertain. Consequently, the Beijing SSA validation should be interpreted as the agreement of the ASI-based retrievals with additionally quality-screened Level 1.5 AERONET inversion products, rather than with fully quality-assured Level 2.0 SSA.

2.3 AI Based ASI Aerosol Retrieval Algorithm

The inversion algorithm developed in this study comprises four main components: clean-sky image processing, image feature extraction, data matching, and the machine learning model. The overall technical framework of the proposed ASI-based aerosol retrieval algorithm is illustrated in Figure 2.

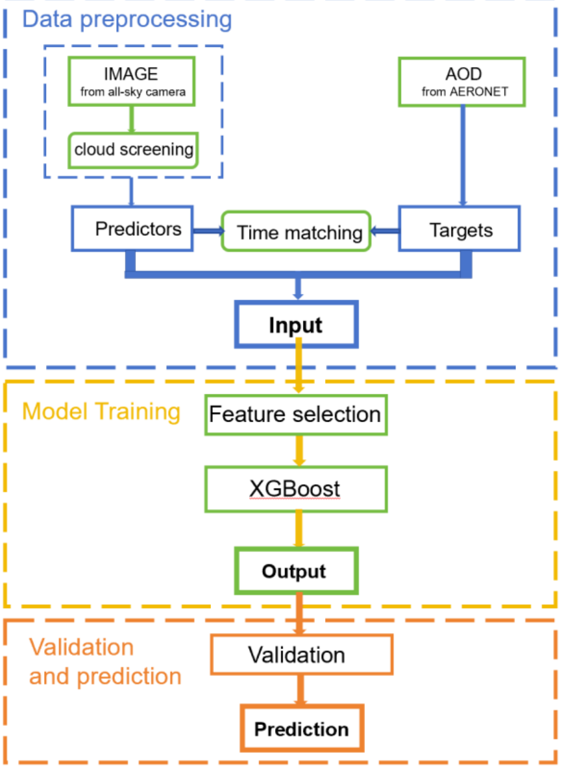

Figure 2: Schematic flowchart of the proposed aerosol retrieval framework.

Clean-Sky Image Processing: Upon acquiring time-stamped raw sky images, we first mask areas that interfere with the extraction of cloud-free sky radiance—namely buildings, clouds, and glare spots caused by the sun and lens artifacts. The specific steps are:

(a) Masking buildings at the image periphery.

(b) Identifying and masking the brightest circular region (sun and its immediate surroundings): the solar center was identified from the grayscale image using an integral-image-based search. A square window with a radius of 45 pixels and a step size of 5 pixels was used to locate the brightest region, and a circular mask with a radius of 220 pixels was applied around the detected solar center. For the TSI images, an additional fixed circular/elliptical mask was applied to remove the instrument support structure.

(c) Cloud and lens flare masking: all-sky images were first converted to grayscale for masking. Cloud-contaminated and other bright regions were removed using an iterative thresholding scheme (Ridler and Calvard, 1978). The initial threshold was set to 150. At each iteration, pixels with non-zero intensities were separated into two groups according to the current threshold: pixels with intensity values greater than the threshold were assigned to the background group, whereas pixels less than or equal to the threshold were assigned to the foreground group. The mean intensities of the two groups were then calculated, and the threshold was updated as the average of the two means. The iteration was stopped when the threshold change was less than or equal to 1. Pixels classified as background were set to zero in the RGB image, producing a cloud-masked image.

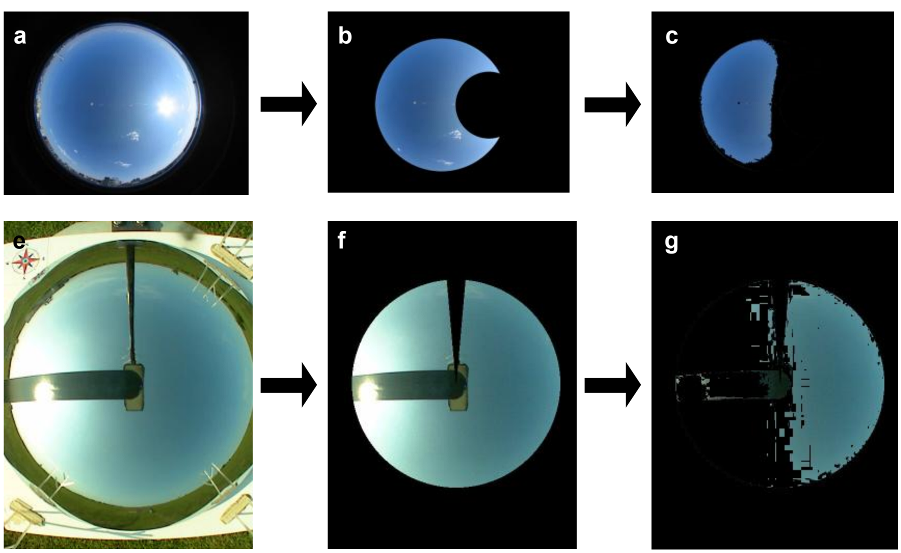

Figure 3: Visualization of the stepwise image processing workflow. The upper panels (a–c) and lower panels (d–f) display representative examples from the Beijing and SGP sites, respectively. From left to right: (a, d) the original raw full-color images; (b, e) the intermediate results after applying geometrical correction and solar disk masking; and (c, f) the final preprocessed images, with non-sky elements removed, ready for aerosol optical property retrieval. Source for (e): ARM user facility (https://adc.arm.gov/discovery/results/instrument_class_code::tsi), licensed under CC BY 4.0 (https://creativecommons.org/licenses/by/4.0/). Last access: 21 April 2026.

While the core retrieval algorithm remains consistent across both sites, a site-specific preprocessing step was implemented for the SGP dataset to account for instrument differences. Unlike the setup at the Beijing site, the Total Sky Imager (TSI) at the SGP site is equipped with a sun occultation system (a sun-blocking strip and support arm) to prevent sensor saturation. This physical structure introduces permanent non-sky artifacts into the field of view. To address this, we applied a fixed fan-shaped digital mask to the SGP raw images prior to cloud screening and feature extraction. This mask effectively assigns zero weights to the pixels occupied by the occultation arm, excluding them from subsequent calculations. Beyond this geometric masking, the entire downstream processing pipeline—including the extraction of statistical features (mean, standard deviation, and texture) and the XGBoost model architecture—remains identical to that applied at the Beijing site, ensuring methodological consistency.

Image Feature Extraction: We extract all colored pixels from the processed sky region image. Each pixel is represented by its Red (R), Green (G), and Blue (B) channel values. The mean values of R, G, and B across all these pixels are computed, and the Red-to-Blue Ratio (RBR) is calculated as the ratio of the R mean to the B mean (Long et al., 2006). Using the image timestamp and geolocation, the solar zenith angle (SZA) is computed. Including SZA is crucial as it explicitly informs the model of the observation geometry, allowing it to decouple the geometrical dependence of sky radiance from aerosol-induced variations. To emulate the sun photometer's Almucantar scanning mode (fixed zenith angle, varying azimuth), a circular annulus with a radius between 0.6 and 0.8 times the sky image radius is defined, centered on the image midpoint. At least 10 pixels are evenly sampled along this annulus to extract their specific RGB values, thereby capturing directional aerosol scattering information. Consequently, the final input feature vector constructed for the XGBoost model comprises the global RGB channel means, the RBR, the SZA, and the discrete RGB values obtained from the annulus sampling points.

The physical basis of these feature groups follows established aerosol radiative transfer and Sun-sky photometer retrieval theory. The global RGB means represent the bulk visible-light response of the cloud-free sky dome. Under clear-sky conditions, increasing aerosol loading attenuates the direct solar beam and modifies the diffuse sky radiance field through aerosol extinction, which is the combined effect of scattering and absorption. Therefore, the mean RGB intensities provide first-order information on aerosol optical depth. The RBR feature further describes the spectral contrast of the sky image. Because the wavelength dependence of aerosol extinction is strongly related to particle size through Mie scattering and is commonly represented by the Angstrom exponent, the red-to-blue contrast can provide size-related information on the relative contribution of fine- and coarse-mode particles (Eck et al., 2010; Schuster et al., 2006). Thus, RBR is not merely an empirical color index, but can serve as an image-derived proxy for the spectral dependence of sky radiance associated with aerosol optical properties, particularly the particle-size-related wavelength dependence of aerosol extinction.

The annulus-sampling features are designed to capture directional scattering information. This design follows the observational concept of AERONET almucantar scans, in which sky radiance is measured at a fixed view zenith angle with varying azimuth angles around the Sun (Dubovik et al., 2000; Dubovik and King, 2000; Sinyuk et al., 2020). Although the ASI annulus is not a fully calibrated almucantar scan, it preserves the key angular-sampling idea by extracting RGB values along a constant radial distance while varying azimuthal direction. The angular distribution of diffuse sky radiance is controlled by aerosol optical depth, the scattering phase function, and single scattering albedo. In particular, sky-radiance inversion methods retrieve aerosol size distribution, refractive index, and SSA by combining spectral AOD with multi-angular sky radiance measurements (Dubovik et al., 2000; Dubovik and King, 2000). Therefore, annulus RGB values provide information related to aerosol scattering angular patterns and absorption, helping the machine-learning model retrieve not only AOD but also SSA. SZA is included to explicitly account for the solar illumination geometry and atmospheric optical path length, allowing the model to distinguish aerosol-induced radiance changes from purely geometrical effects.

Data Matching: Features extracted from the ASI are matched with aerosol optical parameters from the collocated AERONET instruments based on timestamps. A successful match requires the time difference between the AERONET measurement and the ASI image capture to be less than 5 minutes to ensure temporal consistency.

Machine Learning Algorithm: We developed a machine learning inversion method based on the XGBoost model, where model fitting was performed to establish a nonlinear mapping between the input features (observational data) and the target parameters to be inverted (Lary et al., 2016). The Root Mean Square Error (RMSE) was adopted as the loss function to quantify the fitting error and guide the optimization of the model. The optimal number of boosting iterations (N) was determined via 10-fold cross-validation with early stopping (Chai and Draxler, 2014). Using this optimal N and hyperparameters including a maximum tree depth of 7, learning rate of 0.08, subsampling ratio of 0.75, column sampling ratio of 1.00, and minimum loss reduction for leaf node splitting set to 0, the data was used to train the ensemble regression model. To ensure strictly independent validation and assess temporal generalization, the dataset was sorted chronologically. We utilized a time-series splitting strategy where the first two-thirds of data from each month formed the training set, and the subsequent one-third was reserved as the independent test set (Arlot and Celisse, 2009; Roberts et al., 2017). This approach prevents data leakage caused by the high temporal autocorrelation of atmospheric parameters (Karpatne et al., 2017). This strategy also ensures that the model is evaluated on unseen data while maintaining comprehensive seasonal coverage in both subsets.

Following the chronological splitting strategy, the final experimental dataset for the four spectral channels was divided as follows: for the Beijing site, the training and independent test sets comprised 3675 and 2206 samples, respectively; for the SGP site, 1669 samples were used for training and 807 for testing.

This process yielded a model capable of joint output (e.g., SSA at 440 nm, AOD at 440 nm). The trained model was applied to the independent test set to generate predictions. Scatter density plots were constructed with AERONET values on the x-axis and predicted values on the y-axis. Gaussian kernel density estimation was used to visualize point density. A 1:1 reference line (y=x) and a linear regression fit line ($y = ax + b$) were overlaid. The proportionality was quantitatively assessed using the regression slope (k). This procedure was repeated for each of the four wavelength channels (440, 675, 870, 1020 nm), resulting in a trained ensemble regression model for each channel.

3. Results and Discussion

3.1 Overall AOD and SSA retrieval performance by ASI

This section discusses the performance of the model at both the Beijing and SGP sites, evaluating its robustness and reliability across different climatic conditions.

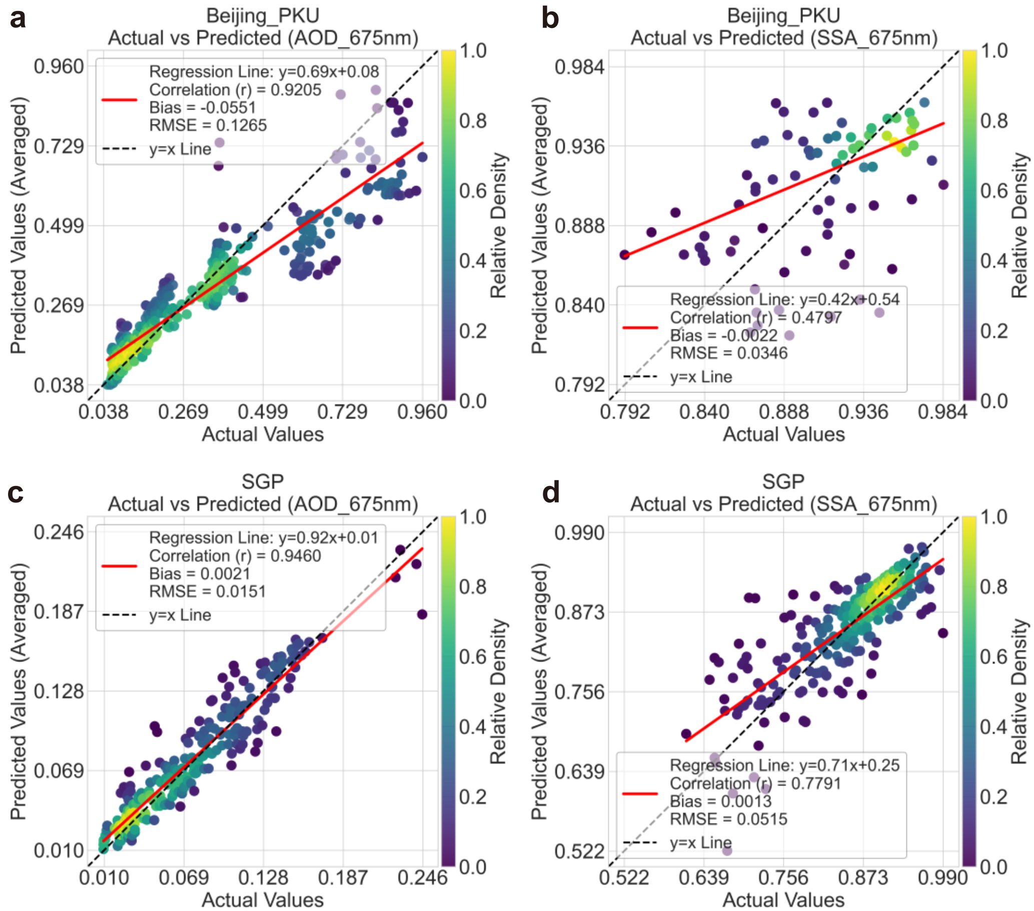

Figure 4: Independent validation results of XGBoost model predictions at 675 nm for the Beijing_PKU site (a, b) and the SGP site (c, d). Scatter plots show averaged predicted values versus actual values for AOD (a, c) and SSA (b, d). The red line represents the linear regression fit, and the black dashed line indicates the 1:1 reference line. Point colors indicate the relative density of observations. Statistical metrics including the Pearson correlation coefficient (r), bias, and root mean square error (RMSE) are shown in each panel.

Figure 4 displays the scatter density plots of AOD and SSA retrieved by the algorithm versus AERONET observations at 675 nm for the Beijing and SGP sites over the entire study period.

Table 1: Statistical summary of retrieval performance, including Pearson Correlation Coefficient (r), Root Mean Square Errors (RMSE), and Mean Absolute Errors (MAE) for AOD and SSA across four spectral channels (440, 675, 870, and 1020 nm). Results are presented for (a, b) the Beijing site and (c, d) the SGP site.

Site	Parameter	Metric	440 nm	675 nm	870 nm	1020 nm
Beijing	AOD	*r*	0.91	0.90	0.91	0.90
		RMSE	0.21	0.12	0.08	0.06
		MAE	0.14	0.08	0.06	0.05
	SSA	*r*	0.69	0.74	0.63	0.48
		RMSE	0.04	0.03	0.03	0.04
		MAE	0.03	0.02	0.03	0.03
SGP	AOD	*r*	0.89	0.91	0.92	0.87
		RMSE	0.05	0.03	0.02	0.02
		MAE	0.03	0.01	0.01	0.01
	SSA	*r*	0.64	0.79	0.83	0.84
		RMSE	0.08	0.06	0.07	0.09
		MAE	0.04	0.04	0.05	0.06

The retrieved AOD agrees well with AERONET AOD, with all data points closely distributed around the 1:1 line. For both sites, the Pearson correlation coefficient (r) for AOD exceeds 0.87 across all wavelengths, demonstrating robust retrieval performance. The retrieval performance for SSA is lower compared to that of AOD, which is not surprising since SSA is highly sensitive to uncertainties in the diffuse measurements (Dubovik et al., 2000).
According to Table 1, for the Beijing site, the model demonstrated robust performance in retrieving AOD across all wavelengths, with r values ranging from 0.90 to 0.91 and RMSE values of 0.06–0.21. SSA retrieval at Beijing showed moderate but wavelength-dependent performance: the correlation was highest at 675 nm ($r = 0.74$) and decreased progressively toward longer wavelengths, reaching $r = 0.480$ at 1020 nm. Despite the low correlation, RMSE remained consistently low (≤ 0.04) across all bands, which may partly be attributed to the narrow dynamic range of SSA values at this site(Legates and McCabe Jr., 1999).
We performed a Monte Carlo sensitivity experiment by adding Gaussian random perturbations to the AOD and SSA training labels. The results show that SSA retrievals are more sensitive to the assumed label uncertainty than AOD retrievals. Under the 0.03 perturbation scenario, SSA RMSE increased from 0.0266 to 0.0299, while under the conservative 0.06 scenario, it increased to 0.04. In contrast, AOD RMSE and correlation do not show a significant positive or negative trend. This indicates that the Beijing SSA retrieval uncertainty is partly constrained by the uncertainty of the Level 1.5 reference data. (Fig. S2)
To further interpret the wavelength-dependent SSA performance at the Beijing_PKU site, we examined the SSA distributions under the clean regime (AOD440 < 0.2; Fig. 5). The sample size is identical at all four wavelengths (N = 657), indicating that the observed differences are not caused by unequal sampling. As shown in Fig. 5(a) and (c), the reference SSA values are concentrated within a relatively narrow high-SSA range, with only limited variation across wavelengths. The mean SSA

decreases slightly toward longer wavelengths, while the interquartile range and 95% confidence interval remain narrow. This range restriction helps explain why the Pearson correlation decreases at longer wavelengths: when the dynamic range of the reference SSA is small, even modest absolute deviations and retrieval uncertainty can lead to a substantial reduction in correlation. Therefore, the weaker long-wavelength SSA correlation at Beijing_PKU should be interpreted primarily as a consequence of limited SSA variability in the clean regime, rather than as evidence of a failure of the ASI-based retrieval to capture the overall SSA magnitude.

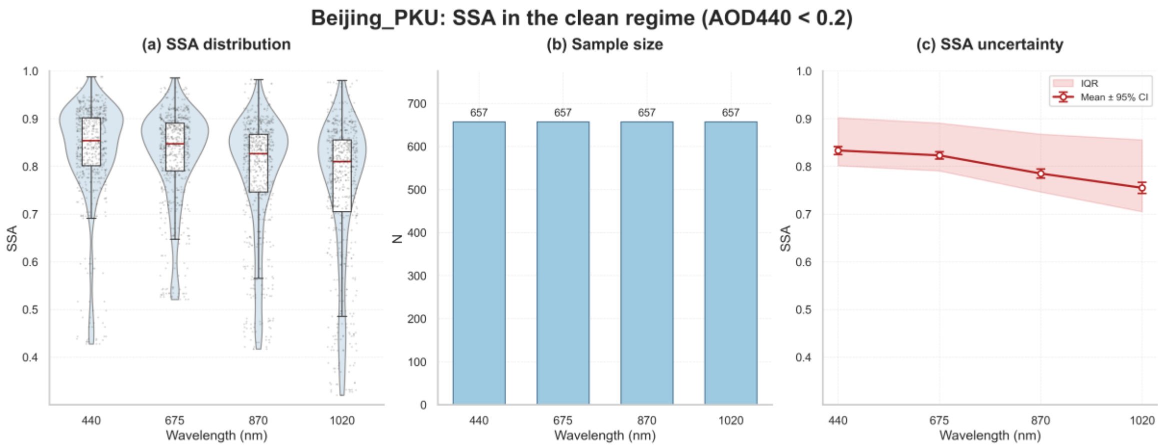

Figure 5: SSA statistics in the clean regime (AOD440 < 0.2) at Beijing_PKU. Panel (a) shows the SSA distribution at four wavelengths, where the violin shape indicates kernel density, the box indicates the median and interquartile range, and the gray dots denote individual samples. Panel (b) shows the sample size at each wavelength. Panel (c) shows the wavelength-dependent SSA mean, 95% bootstrap confidence interval, and interquartile range.

For the SGP site, the model achieved higher overall accuracy than at Beijing. AOD retrieval yielded r values of 0.87–0.92 with notably low RMSE (0.02–0.05), reflecting the more stable aerosol conditions at this site. SSA retrieval also showed improved performance compared to Beijing, with r increasing from 0.64 at 440 nm to 0.84 at 1020 nm and RMSE remaining below 0.09. These evaluation metrics indicate that the algorithm can effectively retrieve AOD and SSA with reasonable accuracy and stability throughout the observation period.

Existing SSA retrieval products provide useful references for assessing the capability and limitations of ASI-based SSA retrievals. AERONET Version 3 remains the ground-based benchmark and provides spectral SSA at 440, 675, 870, and 1020 nm; its Level 2 inversion framework targets an SSA uncertainty of about 0.03 under quality-controlled almucantar/hybrid conditions(Sinyuk et al., 2020). For PARASOL/POLDER-GRASP, which retrieves SSA at 443, 670, 865, and 1020 nm, the 670 nm SSA validation against AERONET gives R = 0.25–0.54 and RMSE = 0.05–0.07 depending on the GRASP configuration, while high-loading scenes (AOD > 1.5) improve to R = 0.814 and RMSE = 0.029 for GRASP/Models (Chen et al., 2020). The current GEMS aerosol product also retrieves SSA at 443 nm, with validation against AERONET SSA at 440 nm showing that, for AOD > 0.4, 42.76% and 67.25% of retrievals fall within the ±0.03 and ±0.05 error bounds, respectively, increasing to 56.61% and 85.70% for AOD > 1.0(Cho et al., 2024). More recently, the Gaofen-5 DPC multi-angle polarimetric retrieval simultaneously derives AOD, SSA, and land DHR; for AOD443 > 0.4, the retrieved SSA has a correlation coefficient of approximately 0.3, RMSE of 0.05–0.08, and only about 40%–45% of retrievals fall within the ±0.03 error envelope (Zhang et al., 2026). Compared with existing SSA retrieval products, the ASI-based retrievals achieve a broadly comparable level of performance, particularly in terms of RMSE. However, because of differences in wavelength, viewing geometry, aerosol loading, reference data quality, and spatial representativeness, this comparison does not imply that ASI retrievals outperform established AERONET or satellite products. Instead, the results suggest that ASI observations can provide complementary, low-cost, high-temporal-resolution local SSA estimates, especially where dense sun-photometer or advanced satellite observations are unavailable.

3.2 Model Performance Under Different Aerosol Loadings

The accuracy of aerosol retrieval is typically associated with aerosol loading. To evaluate the performance of the algorithm more rigorously, we categorized the validation dataset into three regimes based on the reference 440 nm AOD: clean (AOD_{440nm} < 0.2), moderate (0.2 <= AOD_{440nm} < 0.4), and polluted (AOD_{440nm} >= 0.4). Figure 6 illustrates the retrieval performance for 675 nm AOD and SSA across these regimes for both the Beijing and SGP sites. Note that the y-axis scales are unified to facilitate direct comparison.

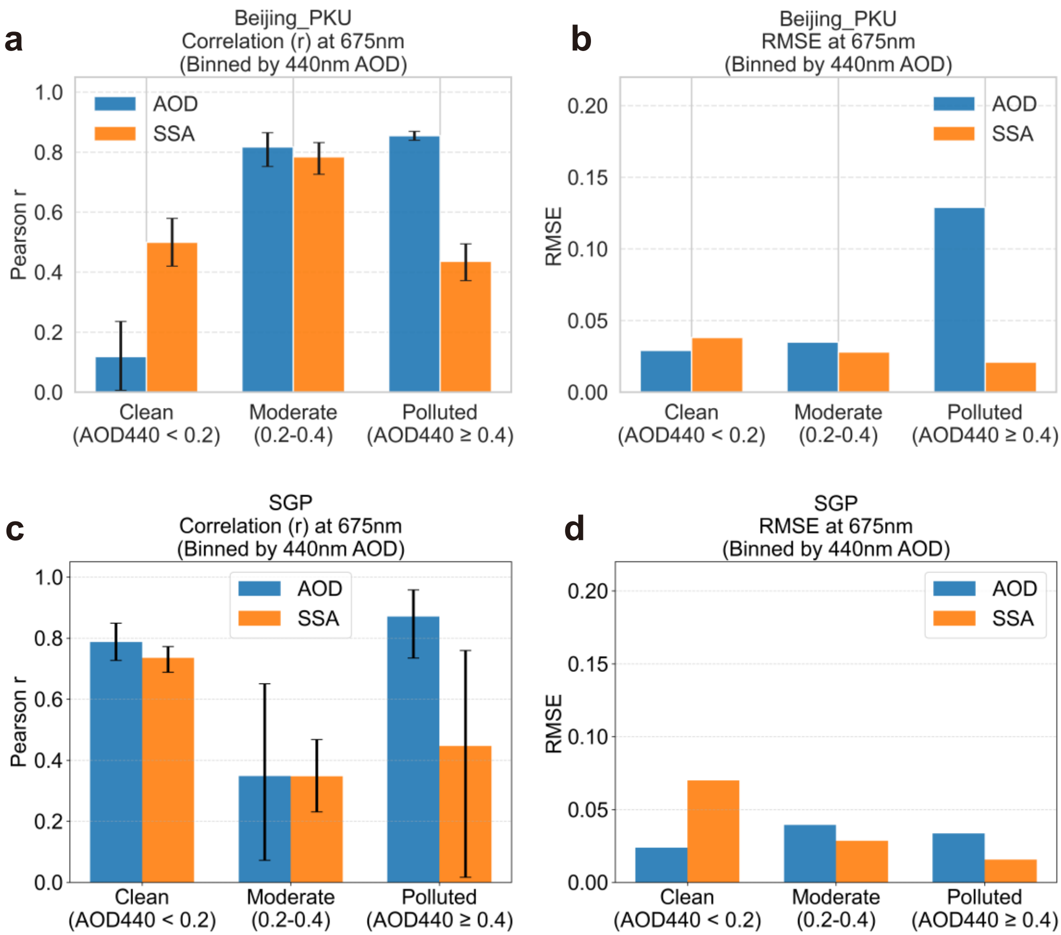

Figure 6: Retrieval performance of AOD and SSA at 675 nm under different aerosol loading regimes for the Beijing_PKU site (a, b) and the SGP site (c, d). The data are binned based on the reference AERONET AOD at 440 nm: Clean (< 0.2), Moderate (0.2 <= AOD440 < 0.4), and Polluted (>= 0.4). The left panels (a, c) display the Pearson correlation coefficient (r) with error bars representing the 95% confidence intervals derived from bootstrap resampling (N = 500). The right panels display the Root Mean Square Error (RMSE).

At the Beijing_PKU site (Fig. 6a-b), the AOD retrieval error exhibits a clear dependence on aerosol loading. In the clean and moderate regimes, the RMSE for AOD remains low (< 0.05). However, in the polluted regime, the RMSE increases significantly to ~0.13. This reflects the challenge of retrieving extremely high aerosol loads in complex urban environments using ASI, where the signal saturation effect may degrade its sensitivity to aerosol loading. However, the RMSE for SSA remains reasonable (< 0.05) across all regimes, confirming that the model correctly estimates the magnitude of absorption even when pixel-level correlation is limited by noise.

The SGP site (Fig. 6c-d) demonstrates superior stability. A striking contrast is observed in the polluted regime: while the AOD RMSE at Beijing surges to 0.13 when AOD > 0.4, the RMSE of AOD at the SGP site remains remarkably low at ~0.035. This is likely related to the fact that the "polluted" conditions at SGP are still optically thinner and less complex than the haze events in Beijing that do not cause image saturation, thus allowing for more accurate retrievals. It should be noted that the relatively low r values observed in the moderate regime for SGP (AOD: $r = 0.34$, SSA: $r = 0.35$) may partly reflect a range restriction effect, as the sample size in this bin is limited (N = 15 in the test set), which can reduce statistical reliability(Jenkins and Quintana-Ascencio, 2020). Despite this, the consistently low RMSE (< 0.05 for AOD and < 0.08 for SSA) across all bins confirms the applicability of ASI in retrieving aerosol properties under cleaner atmospheric background of the Central US.

3.3 Error dependence of SSA retrieval on observing and aerosol conditions

To further characterize the uncertainty of the SSA retrieval, we analyzed how retrieval errors depend on observing geometry, aerosol loading, season, and image brightness (Fig. 7). The residual error was evaluated using RMSE and MAE for SSA at 675 nm in the independent test set at the Beijing_PKU site. The results show that the SSA retrieval error is condition dependent rather than uniform across all samples. The error shows only a weak dependence on SZA between the 50-70° and 70-90° bins, suggesting that the model remains relatively stable over the solar-geometry range represented in the test data. In contrast, the dependence on aerosol loading is more pronounced: the clean regime shows the largest RMSE and MAE, while the moderate and polluted regimes show substantially smaller errors. This is consistent with the limited information content and narrow SSA dynamic range under low-aerosol-loading conditions.

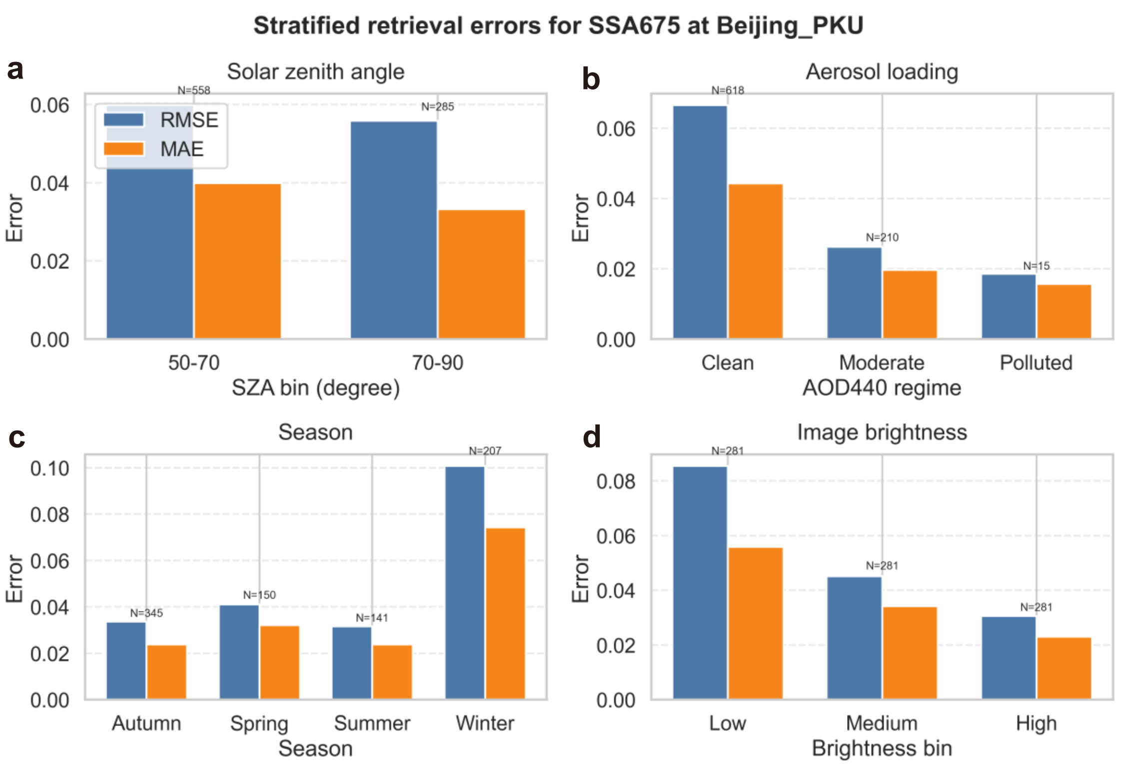

Figure 7. Stratified retrieval errors for SSA at 675 nm in the independent test set at the Beijing_PKU site. The validation samples are grouped by solar zenith angle, aerosol loading, season, and image brightness. Blue and orange bars represent RMSE and MAE,

respectively. The number above each group indicates the sample size. Aerosol loading is classified using AOD at 440 nm, with clean, moderate, and polluted regimes defined as AOD440 < 0.2, 0.2 <= AOD440 < 0.4, and AOD440 >= 0.4, respectively. Image brightness is represented by the mean RGB intensity of the cloud-free sky region and divided into low, medium, and high terciles.

The seasonal analysis further indicates that winter has the largest SSA retrieval error, whereas autumn, spring, and summer show lower and more comparable errors. This may reflect seasonal differences in aerosol type, illumination geometry, and surface-atmosphere conditions that are not fully represented by the current feature set. Image brightness also shows a clear error dependence, with the largest RMSE and MAE occurring in the low-brightness bin and progressively smaller errors under medium and high brightness conditions. This suggests that low image brightness reduces the radiometric contrast available to the model and increases the uncertainty of SSA retrieval. Overall, Fig. 7 indicates that the ASI-based SSA retrieval uncertainty depends on observing and aerosol conditions, which should be considered when extending the method to broader low-cost monitoring networks.

3.4 Sensitivity to Day-Block Temporal Split

To further test whether the retrieval skill could be influenced by short-term temporal autocorrelation, we conducted an additional sensitivity experiment using a day-block temporal split. In this experiment, matched ASI and AERONET samples were grouped by calendar day, and all observations from the same day were assigned exclusively to either the training set or the test set. Approximately two-thirds of the days were used for training and the remaining one-third for testing. The model architecture, input features, and hyperparameters were kept unchanged. The evaluation criteria and aerosol-loading bins were kept identical to those used in Fig. 7, allowing a direct comparison between the baseline within-month chronological split and the day-block split.

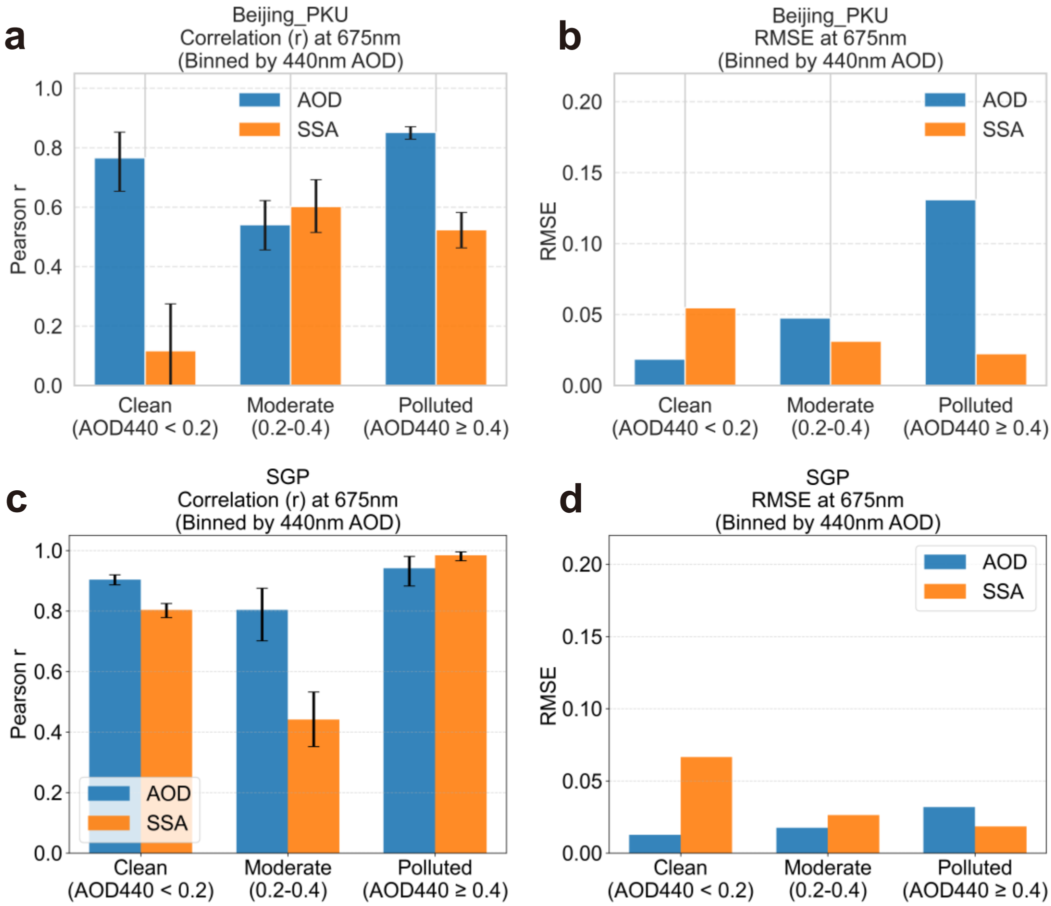

Figure 8: Sensitivity of AOD and SSA retrievals to a day-block temporal split at 675 nm for the Beijing_PKU and SGP sites. Samples were grouped by calendar day, and no day contributed observations to both the training and test sets. The left panels (a, c) show Pearson correlation coefficient (r), and the right panels (b, d) show RMSE for AOD and SSA across clean, moderate, and polluted regimes defined by 440 nm AOD. Error bars indicate 95% confidence intervals obtained by bootstrap resampling.

Compared with the baseline chronological split in Fig. 6, the day-block split in Fig. 8 yields broadly consistent retrieval performance. At the Beijing_PKU site, AOD remains robust across aerosol-loading regimes, although the polluted-bin correlation decreases slightly under the stricter split. SSA shows larger variability, particularly in the polluted regime, which is expected given its narrower dynamic range and stronger sensitivity to sample size. At SGP, the model continues to show strong cross-day generalization, with high correlations and low RMSE for both AOD and SSA. Overall, these results demonstrate that the proposed model retains meaningful predictive capability even under a more stringent temporal validation strategy, supporting the conclusion that the retrieval skill is not primarily caused by local temporal leakage.

3.5 Evaluation of Diurnal Variability

A major advantage of ASI is the capability to retrieve aerosol properties with high temporal resolution, thus allowing for the representation of aerosol diurnal cycle. Here we first selected June 15, 2017 at Beijing site as a representative case since AOD on this day exhibited significant intra-day variation, providing an ideal condition for testing the model performance.

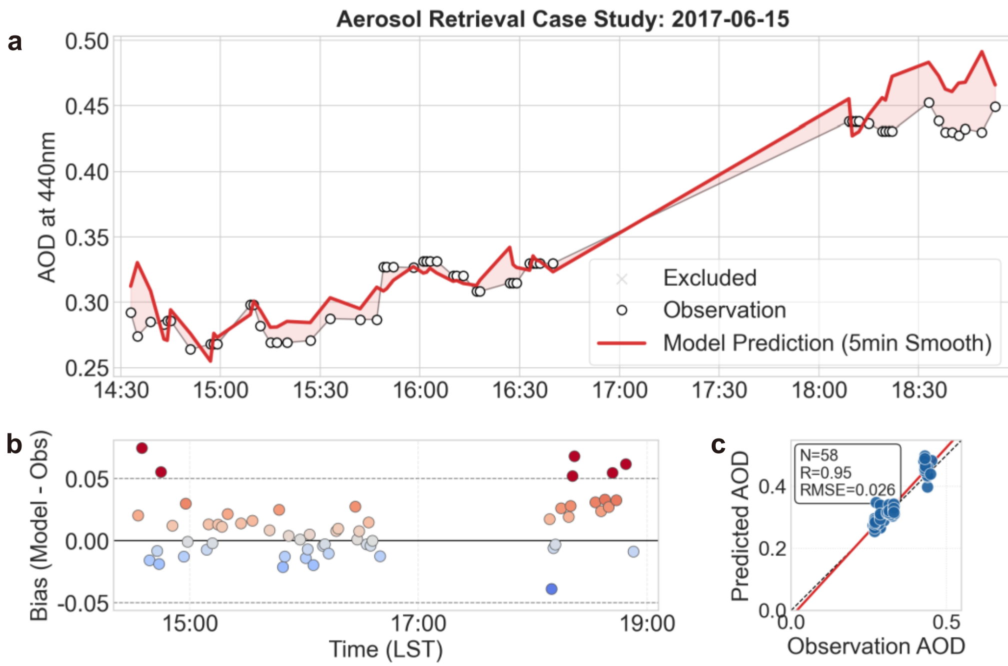

Figure 9: Case study of diurnal AOD variation retrieval at the Beijing site on June 15, 2017. The top panel (a) compares the AERONET observations (black circles) with the model predictions that have not been independently validated (red solid line, smoothed using a 5-minute time window). The bottom panels display the time series of retrieval bias (b) and the scatter plot between observed and predicted AOD (c). For visualization only, a 5-minute moving average was applied to the ASI retrievals in Fig. 9a to reduce point-to-point noise and highlight the overall diurnal trend. All statistical metrics reported in this study, however, were calculated from the original unsmoothed retrievals.

As shown in the time series (Fig. 9a), the ASI retrieved AOD demonstrates remarkable consistency with ground-based AERONET observations. Note that a 5-minute time window smoothing technique was applied to the ASI AOD curve (red line) to filter out high-frequency retrieval noise. However, all statistical metrics reported in this study were calculated using the original, unsmoothed retrieval results to ensure rigorous validation. The ASI retrievals accurately capture the trend of AOD diurnal variability. AOD gradually increased and fluctuated from 15:00 to 18:00, and then stabilized, which is well captured by the ASI. While the observations showed a "stepped" pattern due to instrument sampling characteristics, the model retrieval (solid red line) successfully fitted the central tendency of these discrete points. Moreover, the model responds sensitively to rapid changes, demonstrating its sensitivity to short-term high-frequency variations in atmospheric aerosols.

The statistical metrics (Fig. 9c) further confirm the retrieval accuracy. With 58 sample points, the correlation coefficient (R) reached 0.95, and the Root Mean Square Error (RMSE) was only 0.03.

The bias analysis (Fig. 9b) shows that the deviations for most data points were confined within ± 0.03. Although minor overestimation occurred in the low-value period around 14:30 and 18:30, the overall bias distribution remained balanced without significant systematic errors.

The 5 min moving average in Fig. 9 was used only for visual clarity, whereas the statistical metrics were calculated from the unsmoothed ASI retrievals. To quantify the smoothing effect, we calculated the difference between the raw ASI retrievals and the 5 min moving average for the case (Fig. S1). The mean difference was 0.0008, indicating no systematic bias introduced by smoothing. The standard deviation of the difference was 0.01, the mean absolute difference was 0.0076, and the 95th percentile absolute difference was 0.03. These values are much smaller than the daytime AOD variation shown in Fig. 9, suggesting that the 5 min smoothing mainly suppresses high-frequency noise while preserving the diurnal variation pattern.

It is worth noting that a similar high-frequency diurnal analysis was not performed for SSA. Unlike AOD, which is derived from high-frequency direct sun measurements, SSA is retrieved from the much less frequent almucantar sky scans. This significantly reduces the number of valid SSA data points, making it unfeasible to characterize continuous intra-day variations. Similarly, such high-frequency analysis is also not available at the SGP site for either parameter.

We continue to explore the averaged diurnal cycles of AOD and SSA retrieved by ASI. We select the Beijing_PKU site using data from May 2017 to May 2018. This one-year period was selected to ensure complete seasonal coverage while maintaining sufficient sample size within each seasonal group. All matched data from the independent test set within this period were grouped by season — Spring (Mar–May), Summer (Jun–Aug), Autumn (Sep–Nov), and Winter (Dec–Feb) — and the hourly mean and standard deviation of both AERONET observations and model retrievals were calculated within each seasonal group. All timestamps were converted from UTC to Beijing Local Standard Time (LST, UTC+8) prior to analysis. It should be noted that the diurnal coverage is confined to approximately 12:00–18:00 LST, corresponding to the period of direct solar illumination required for valid AERONET almucantar sky scan retrievals, which limits the representativeness of the full diurnal cycle but still captures the afternoon period.

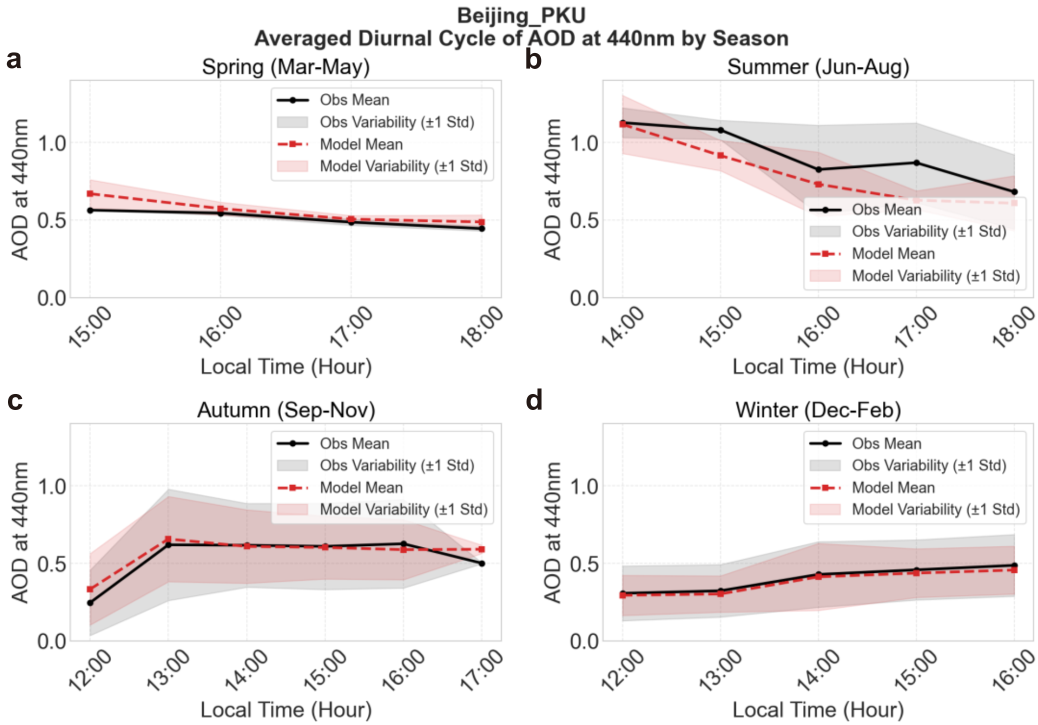

Figure 10: Averaged diurnal cycles of AOD at 440 nm at the Beijing_PKU site, stratified by season: (a) Spring (Mar–May), (b) Summer (Jun–Aug), (c) Autumn (Sep–Nov), and (d) Winter (Dec–Feb). Black solid lines and gray shading represent the AERONET observed hourly means and ±1 standard deviation, respectively. Colored dashed lines and shading indicate the means and variability of the corresponding model retrieval results. The diurnal coverage is limited to afternoon hours due to the temporal overlap between ASI acquisition and AERONET measurement windows.

Figure 10 presents the averaged diurnal cycles of AOD at 440 nm at the Beijing_PKU site across four seasons (12:00–18:00 LST). A clear seasonal contrast is observed in the AOD magnitude, with summer exhibiting the highest loading and the largest diurnal variability, while winter shows the lowest values and the most stable diurnal pattern. In spring, both the observed and retrieved AOD display a slight decreasing trend from 15:00 to 18:00 LST, and the model closely follows the observed afternoon evolution. In summer, AOD decreases gradually from the early afternoon toward 18:00 LST, and the model captures the overall downward tendency, although a small underestimation appears around the late-afternoon period. In autumn, AOD increases sharply from 12:00 to 13:00 LST and then remains relatively stable through most of the afternoon before decreasing slightly at 17:00 LST; the model reproduces this pattern well, including the elevated values around 13:00 LST. In winter, the diurnal cycle is weak, with AOD increasing slowly and smoothly from noon to 16:00 LST, and the model remains in good agreement with the observations throughout the period. Overall, the retrievals successfully reproduce the seasonal differences in both magnitude and afternoon variability, with observation and model uncertainty ranges overlapping in most time bins.

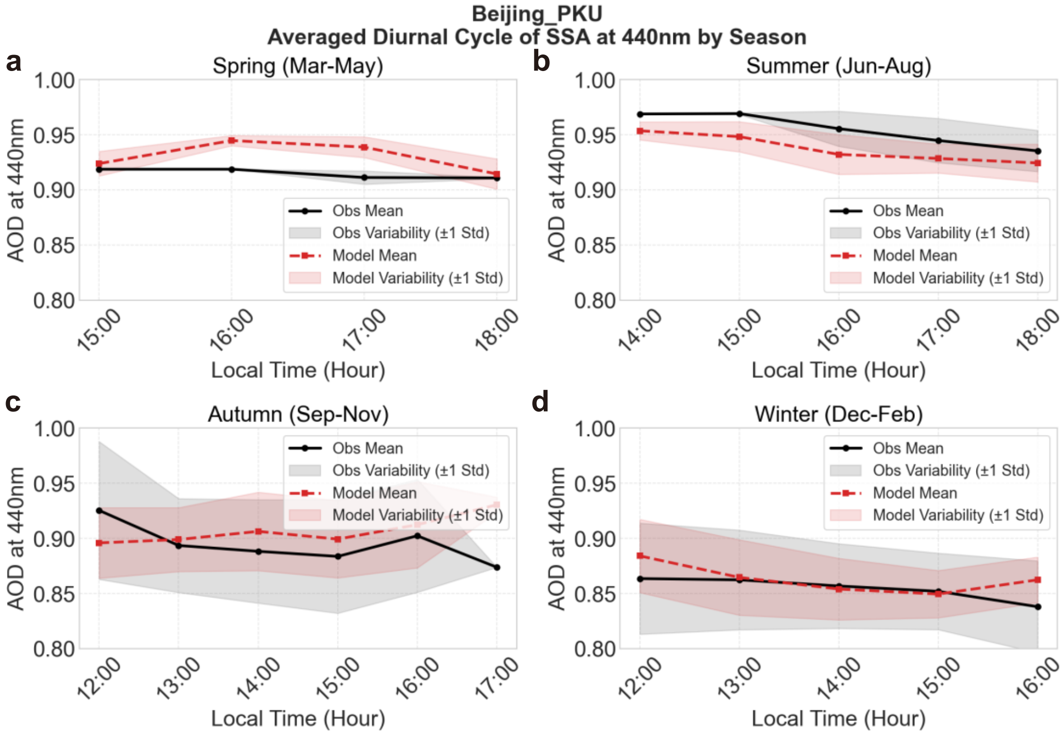

Figure 11: Same as Figure 10 but for SSA at 440 nm.

Figure 11 shows the corresponding diurnal cycles of SSA at 440 nm. SSA exhibits smaller diurnal variation compared to AOD across all seasons. In spring, the model systematically overestimates SSA by approximately 0.03, indicating a tendency to underestimate aerosol absorption. Summer shows similar underestimation behavior in the early afternoon. Winter performance is the best among all seasons, with the model mean closely tracking observations throughout the afternoon. Autumn shows the largest retrieval uncertainty and a diverging trend between observations and model after 16:00 LST, though the wide uncertainty bands suggest this may partly reflect high day-to-day variability rather than a systematic model bias.

3.6 Evaluation of Seasonal Variability

While Section 3.3 focuses on daily scale consistency, the following section further examines the temporal stability of the retrievals at seasonal scales for the Beijing and SGP sites, respectively.

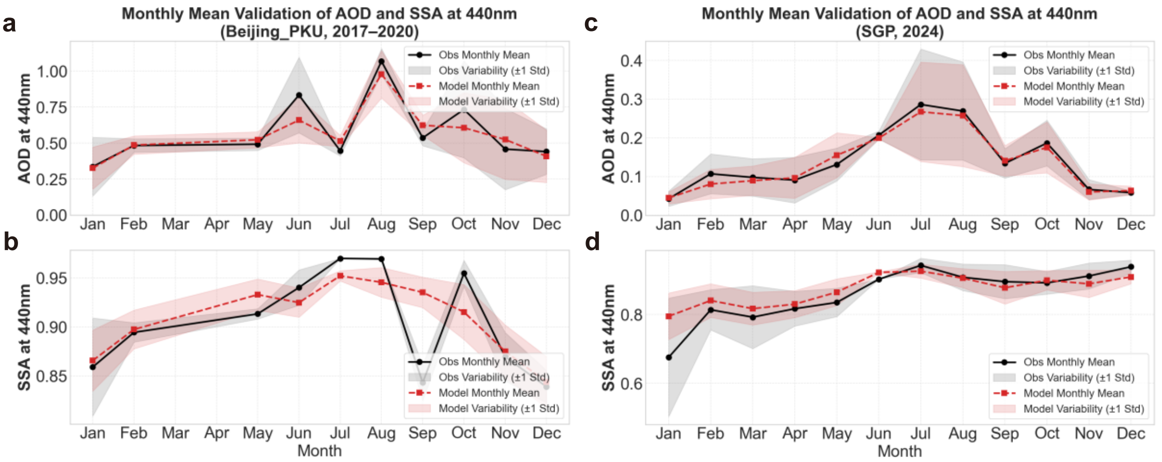

Figure 12: Monthly mean validation of AOD (upper panels) and SSA (lower panels) at 440 nm at the Beijing_PKU site (a, b) and the SGP site (c, d). Black solid lines and gray shading denote the monthly means and ±1 standard deviation of AERONET observations, respectively. Red dashed lines and pink shading represent the corresponding model retrieval means and variability. The standard deviation reflects the variability of all matched observations within each month across the full study period (Beijing: 2017–2020; SGP: 2024).

Figure 12 presents the monthly mean validation of AOD and SSA at 440 nm for both the Beijing_PKU and SGP sites. Overall, the model reproduces the seasonal cycles of both parameters at both sites reasonably well, with the monthly means generally tracking the observed values throughout the year.

For AOD at the Beijing site (Fig. 12a), the seasonal cycle is well captured, with relatively low values in winter and spring, a pronounced enhancement in early summer, and the highest monthly mean in August. The model agrees well with the observations during most months, but it tends to underestimate the summer peak, especially in June and August, and slightly smooths the sharp month-to-month transition from summer to early autumn. For SSA at Beijing (Fig. 12b), the model follows the observed seasonal evolution, with high SSA values from spring to summer and a decrease in early autumn. However, the model is less sensitive to the abrupt SSA reduction around September and shows a smoother monthly cycle than the observations, indicating that the most rapid month-to-month changes are only partially captured.

At the SGP site, both AOD and SSA show good seasonal consistency between model and observations for most of the year. For AOD (Fig. 12c), the model closely follows the observed seasonal peak in summer and the low values in winter, with only a slight underestimation of 0.02–0.05 during January–April. It is worth noting that June exhibits negligible variability in both observations and model retrievals (indicated by the near-absent shading), which is attributable to the extremely limited number of valid matched samples in that month — with only a single observation day available — rather than reflecting genuinely low aerosol variability. This should be considered when interpreting the June monthly mean. For SSA (Fig. 12d), the model performs well from June to December, with the two lines nearly overlapping and the uncertainty ranges mutually covering each other. However, a notable overestimation is observed in January, where the model predicts ~0.80 while the observed SSA is only ~0.68. Overall, the monthly means demonstrate that the method captures the broad seasonal evolution of both AOD and SSA at both sites, although the retrievals are less sensitive to abrupt month-to-month transitions and low-sample months.

4. Summary and Outlook

This study successfully constructed an XGBoost regression model based on visible-band image features from an All-Sky Imager and AERONET ground-based measurements, enabling the simultaneous retrieval of AOD and SSA across four spectral channels (440, 675, 870, 1020 nm). This approach replaces the iterative computation of traditional physical models with a data-driven, nonlinear mapping between sky radiance features and aerosol optical parameters, addressing a research gap in multi-dimensional aerosol parameter retrieval from ASIs. Compared with previous ASI-based machine-learning studies that mainly retrieved AOD and size-related parameters, the main methodological contribution of this work is the simultaneous retrieval of AOD and SSA from RGB sky-camera imagery. The SSA retrieval expands the potential use of ASIs from aerosol loading estimation toward absorption-related aerosol characterization.

The model demonstrated high reliability across all spectral bands. AOD retrievals showed the best performance, with Pearson correlation coefficients (r) exceeding 0.86 across all wavelengths at both sites, RMSE ranging from 0.02 to 0.25, and mean absolute errors (MAE) below 0.15. SSA retrievals exhibited moderate but wavelength- and site-dependent performance: at the Beijing_PKU site, r decreased from 0.67 at 440 nm to 0.33 at 1020 nm, while at the SGP site, r increased from 0.64 at 440 nm to 0.84 at 1020 nm. RMSE for SSA remained consistently low (≤ 0.09) across all bands and both sites, suggesting that the model can reproduce SSA magnitudes, although the Beijing SSA validation is limited by the use of Level 1.5 AERONET reference products and by the narrow dynamic range of SSA.

Previous ASI-based retrieval studies have demonstrated promising AOD accuracy, with correlation coefficients exceeding 0.92 and MAE below 0.005 using machine learning approaches, or r^2 of approximately 0.87 using radiative transfer inversion with the GRASP code. However, these methods are either restricted to AOD and Angström exponent retrieval, or rely on computationally intensive radiative transfer iterations, and none has demonstrated simultaneous SSA retrieval. Compared to traditional radiative transfer model iteration methods, the method achieves comparable AOD accuracy ($r > 0.86$, RMSE < 0.05 at the SGP site) while simultaneously retrieving SSA for the first time using ASI imagery, representing a promising extension of ASI-based aerosol remote sensing capabilities. Furthermore, the data-driven XGBoost framework significantly reduces computational overhead compared to iterative radiative transfer approaches, making it well-suited to the high temporal resolution of all-sky imagers. Because ASIs are relatively low-cost and easy to maintain, the proposed method has potential value as a complementary approach for future dense aerosol monitoring. However, the present validation is limited to two sites and selected observation periods. Therefore, the current results should be regarded as a proof of concept rather than evidence of operational generalizability. Further evaluation across different ASI instruments, calibration conditions, surface types, seasons, aerosol mixtures, and cloud-screening environments is required before the method can be used as a robust network-scale aerosol product.

This study holds both theoretical and practical significance. On a theoretical level, the all-sky image feature-to-multi-optical-parameter mapping model established in this work enriches the machine learning application paradigm in aerosol remote sensing and provides methodological references for inversion studies integrating multi-source data. On a practical level, the approach can be directly applied in scenarios such as solar power plants and remote ecological reserves: high spatiotemporal resolution coordinated observations of AOD and SSA can be used to assess the impact of aerosols on surface solar radiation. Meanwhile, this study has two main aspects open for improvement. First, the data coverage does not include samples from extreme environments such as high-latitude regions and deserts, thus the global generalizability of the conclusions requires further validation. Second, the lack of integrated aerosol vertical distribution information prevents the distinction of parameter differences between the boundary layer and the free atmosphere. In the future, we will continue to explore the applicability of ASI in retrieving different aerosol parameters as well as under different environments.

Data Availability Statement

The datasets used and analyzed during the current study are available from various sources. The all-sky imager (ASI) data collected at the Beijing_PKU site are proprietary to our research group and are available from the corresponding author upon reasonable request. The ASI images for the Southern Great Plains (SGP) site are publicly available through the Atmospheric Radiation Measurement (ARM) user facility data archive (https://adc.arm.gov/discovery/). Additionally, the reference aerosol optical parameters can be accessed via the Aerosol Robotic Network (AERONET) database (https://aeronet.gsfc.nasa.gov/).

Author contributions

J.L. conceptualized the research, and provided overall supervision. H.N. was responsible for the research design, performing the experiments, data collection and processing, and drafting the manuscript. Z.Z. provided the essential data for the study. L.C., Y.D., G.D., M.L., Q.L., G.L., Y.S., A.T., S.Y. and C.Z. contributed to the maintenance and management of the instruments. J.L. and H.N. performed the data analysis and results discussion, contributed to the critical revision of the manuscript and approved the final version.

Competing interests

The authors declare that a patent application related to the method described in this manuscript has been filed by Peking University (Application No. CN202511448418.3). The authors have no other competing interests.

Acknowledgements

This study is funded by the National Natural Science Foundation of China (Grant No. 42425503 and 42375121) and the Beijing Natural Science Foundation (Grant No. QY25158).

References

Arlot, S. and Celisse, A.: A Survey of Cross Validation Procedures for Model Selection, Statistics Surveys, 4, https://doi.org/10.1214/09-SS054, 2009.

Bellouin, N., Quaas, J., Gryspeerdt, E., Kinne, S., Stier, P., Watson-Parris, D., Boucher, O., Carslaw, K. S., Christensen, M., Daniau, A.-L., Dufresne, J.-L., Feingold, G., Fiedler, S., Forster, P., Gettelman, A., Haywood, J. M., Lohmann, U., Malavelle, F., Mauritsen, T., McCoy, D. T., Myhre, G., Mülmenstädt, J., Neubauer, D., Possner, A., Rugenstein, M., Sato, Y., Schulz, M., Schwartz, S. E., Sourdeval, O., Storelvmo, T., Toll, V., Winker, D., and Stevens, B.: Bounding Global Aerosol Radiative Forcing of Climate Change, Reviews of Geophysics, 58, e2019RG000660, https://doi.org/10.1029/2019RG000660, 2020.

Boucher, O., Randall, D., Artaxo, P., Bretherton, C., Feingold, G., Forster, P., Kerminen, V.-M., Kondo, Y., Liao, H., Lohmann, U., Rasch, P., Satheesh, S., Sherwood, S., Stevens, B., and Zhang, X.: Clouds and Aerosols, 571–892, 2013.

Cazorla, A., Shields, J. E., Karr, M. E., Olmo, F. J., Burden, A., and Alados-Arboledas, L.: Technical Note: Determination of aerosol optical properties by a calibrated sky imager, Atmos. Chem. Phys., 9, 6417–6427, https://doi.org/10.5194/acp-9-6417-2009, 2009.

Chai, T. and Draxler, R. R.: Root mean square error (RMSE) or mean absolute error (MAE)? – Arguments against avoiding RMSE in the literature, Geoscientific Model Development, 7, 1247–1250, https://doi.org/10.5194/gmd-7-1247-2014, 2014.

Chen, C., Dubovik, O., Fuertes, D., Litvinov, P., Lapyonok, T., Lopatin, A., Ducos, F., Derimian, Y., Herman, M., Tanré, D., Remer, L. A., Lyapustin, A., Sayer, A. M., Levy, R. C., Hsu, N. C., Descloitres, J., Li, L., Torres, B., Karol, Y., Herrera, M., Herreras, M., Aspetsberger, M., Wanzenboeck, M., Bindreiter, L., Marth, D., Hangler, A., and Federspiel, C.: Validation of GRASP algorithm product from POLDER/PARASOL data and assessment of multi-angular polarimetry potential for aerosol monitoring, Earth System Science Data, 12, 3573–3620, https://doi.org/10.5194/essd-12-3573-2020, 2020.

Chen, T. and Guestrin, C.: XGBoost: A Scalable Tree Boosting System, in: Proceedings of the 22nd ACM SIGKDD International Conference on Knowledge Discovery and Data Mining, KDD ’16: The 22nd ACM SIGKDD International Conference on Knowledge Discovery and Data Mining, 785–794, https://doi.org/10.1145/2939672.2939785, 2016.

Cho, Y., Kim, J., Go, S., Kim, M., Lee, S., Kim, M., Chong, H., Lee, W.-J., Lee, D.-W., Torres, O., and Park, S. S.: First atmospheric aerosol-monitoring results from the Geostationary Environment Monitoring Spectrometer (GEMS) over Asia, Atmospheric Measurement Techniques, 17, 4369–4390, https://doi.org/10.5194/amt-17-4369-2024, 2024.

Cook, D. and Sullivan, R.: Energy Balance Bowen Ratio (EBBR) Instrument Handbook, 2025.

Dubovik, O. and King, M. D.: A flexible inversion algorithm for retrieval of aerosol optical properties from Sun and sky radiance measurements, J. Geophys. Res., 105, 20673–20696, https://doi.org/10.1029/2000JD900282, 2000.

Dubovik, O., Smirnov, A., Holben, B., King, M., Kaufman, Y. J., Eck, T., and Slutsker, I.: Accuracy assessment of aerosol optical properties retrieved from Aerosol Robotic Network (AERONET) Sun and sky radiance measurements, Journal of Geophysical Research, 105, 9791–9806, https://doi.org/10.1029/2000JD900040, 2000.

Eck, T., Holben, B., Sinyuk, A., Pinker, R., Goloub, P., Chen, H., Chatenet, B., Li, zs, Singh, R., Tripathi, S., Reid, J., Giles, D., Dubovik, O., O'Neill, N., Smirnov, A., Wang, P., and Xia, X.: Climatological aspects of the optical properties of fine/coarse mode aerosol mixtures, Journal of Geophysical Research (Atmospheres), 115, 19205, https://doi.org/10.1029/2010JD014002, 2010.

García, R. D., Barreto, Á., Rey, C., Fraile-Nuez, E., González-Vega, A., León-Luis, S. F., Alcantara, A., Almansa, A. F., Guirado-Fuentes, C., González-Sicilia, P., Cachorro, V. E., and Bouchar, F.: Aerosol retrievals derived from a low-cost Calitoo sun-photometer taken on board a research vessel, Atmospheric Environment, 341, 120888, https://doi.org/10.1016/j.atmosenv.2024.120888, 2025.

Ghonima, M. S., Urquhart, B., Chow, C. W., Shields, J. E., Cazorla, A., and Kleissl, J.: A method for cloud detection and opacity classification based on ground based sky imagery, Atmos. Meas. Tech., 5, 2881–2892, https://doi.org/10.5194/amt-5-2881-2012, 2012.

Hansen, J., Sato, M., and Ruedy, R.: Radiative forcing and climate response, Journal of Geophysical Research: Atmospheres, 102, 6831–6864, https://doi.org/10.1029/96JD03436, 1997.

Hao, H., Wang, K., Zhao, C., Wu, G., and Li, J.: Visibility-derived aerosol optical depth over global land from 1959 to 2021, Earth System Science Data, 16, 3233–3260, https://doi.org/10.5194/essd-16-3233-2024, 2024.

Holben, B. N., Eck, T. F., Slutsker, I., Tanré, D., Buis, J. P., Setzer, A., Vermote, E., Reagan, J. A., Kaufman, Y. J., Nakajima, T., Lavenu, F., Jankowiak, I., and Smirnov, A.: AERONET—A Federated Instrument Network and Data Archive for Aerosol Characterization, Remote Sensing of Environment, 66, 1–16, https://doi.org/10.1016/S0034-4257(98)00031-5, 1998.

Huo, J. and Lü, D.: Preliminary retrieval of aerosol optical depth from all-sky images, Advances in Atmospheric Sciences, 27, 421–426, https://doi.org/10.1007/s00376-009-8216-2, 2010.

Intergovernmental Panel On Climate Change (Ipcc): Climate Change 2021 – The Physical Science Basis: Working Group I Contribution to the Sixth Assessment Report of the Intergovernmental Panel on Climate Change, 1st ed., Cambridge University Press, https://doi.org/10.1017/9781009157896, 2023.

Jenkins, D. and Quintana-Ascencio, P.: A solution to minimum sample size for regressions, PLOS ONE, 15, e0229345, https://doi.org/10.1371/journal.pone.0229345, 2020.

Karpatne, A., Ebert-Uphoff, I., Ravela, S., Babaie, H., and Kumar, V.: Machine Learning for the Geosciences: Challenges and Opportunities, IEEE Transactions on Knowledge and Data Engineering (in review), 31, https://doi.org/10.1109/TKDE.2018.2861006, 2017.

Kazantzidis, A., Tzoumanikas, P., Bais, A. F., Fotopoulos, S., and Economou, G.: Cloud detection and classification with the use of whole-sky ground-based images, Atmospheric Research, 113, 80–88, https://doi.org/10.1016/j.atmosres.2012.05.005, 2012.

Kazantzidis, A., Tzoumanikas, P., Nikitidou, E., Salamalikis, V., Wilbert, S., and Prahl, C.: Application of simple all-sky imagers for the estimation of aerosol optical depth, SOLARPACES 2016: International Conference on Concentrating Solar Power and Chemical Energy Systems, 140012, https://doi.org/10.1063/1.4984520, 2017.

Lary, D. J., Alavi, A. H., Gandomi, A. H., and Walker, A. L.: Machine learning in geosciences and remote sensing, Geoscience Frontiers, 7, 3–10, https://doi.org/10.1016/j.gsf.2015.07.003, 2016.

Legates, D. R. and McCabe Jr., G. J.: Evaluating the use of "goodness-of-fit" Measures in hydrologic and hydroclimatic model validation, Water Resources Research, 35, 233–241, https://doi.org/10.1029/1998WR900018, 1999.

Levy, R. C., Mattoo, S., Munchak, L. A., Remer, L. A., Sayer, A. M., Patadia, F., and Hsu, N. C.: The Collection 6 MODIS aerosol products over land and ocean, Atmospheric Measurement Techniques, 6, 2989–3034, https://doi.org/10.5194/amt-6-2989-2013, 2013.

Li, Z., Guo, J., Ding, A., Liao, H., Liu, J., Sun, Y., Wang, T., Xue, H., Zhang, H., and Zhu, B.: Aerosol and boundary-layer interactions and impact on air quality, National Science Review, 4, 810–833, https://doi.org/10.1093/nsr/nwx117, 2017.

Logothetis, S.-A., Giannaklis, C.-P., Salamalikis, V., Tzoumanikas, P., Raptis, P.-I., Amiridis, V., Eleftheratos, K., and Kazantzidis, A.: Retrieval of Aerosol Optical Properties via an All-Sky Imager and Machine Learning: Uncertainty in Direct Normal Irradiance Estimations, https://doi.org/10.3390/environsciproc2023026133, 2023.

Long, C. N., Sabburg, J. M., Calbó, J., and Pagès, D.: Retrieving Cloud Characteristics from Ground-Based Daytime Color All-Sky Images, Journal of Atmospheric and Oceanic Technology, 23, 633–652, https://doi.org/10.1175/JTECH1875.1, 2006.

Olmo, F., Cazorla, A., Arboledas, L., López-Álvarez, M., Hernández-Andrés, J., and Romero, J.: Retrieval of the optical depth using an all-sky CCD camera, Applied Optics, 47, H182–H189, https://doi.org/10.1364/AO.47.00H182, 2008.

Ridler, T. W. and Calvard, S.: Picture Thresholding Using an Iterative Selection Method, IEEE Transactions on Systems, Man, and Cybernetics, 8, 630–632, https://doi.org/10.1109/TSMC.1978.4310039, 1978.

Roberts, D. R., Bahn, V., Ciuti, S., Boyce, M. S., Elith, J., Guillera-Arroita, G., Hauenstein, S., Lahoz-Monfort, J. J., Schröder, B., Thuiller, W., Warton, D. I., Wintle, B. A., Hartig, F., and Dormann, C. F.: Cross-validation strategies for data with temporal, spatial, hierarchical, or phylogenetic structure, Ecography, 40, 913–929, https://doi.org/10.1111/ecog.02881, 2017.

Román, R., Antuña-Sánchez, J. C., Cachorro, V. E., Toledano, C., Torres, B., Mateos, D., Fuertes, D., López, C., González, R., Lapionok, T., Herreras-Giralda, M., Dubovik, O., and de Frutos, Á. M.: Retrieval of aerosol properties using relative radiance measurements from an all-sky camera, Atmospheric Measurement Techniques, 15, 407–433, https://doi.org/10.5194/amt-15-407-2022, 2022.

Rossini, E. G. and Krenzinger, A.: Maps of sky relative radiance and luminance distributions acquired with a monochromatic CCD camera, Solar Energy, 81, 1323–1332, https://doi.org/10.1016/j.solener.2007.06.013, 2007.

Sabburg, J. and Wong, J.: Evaluation of a Ground-Based Sky Camera System for Use inSurface Irradiance Measurement, J. Atmos. Oceanic Technol., 16, 752–759, https://doi.org/10.1175/1520-0426(1999)016%3C0752:EOAGBS%3E2.0.CO;2, 1999.

Scarlatti, F., Gómez-Amo, J., C. Valdelomar, P., Estellés, V., and Utrillas, M.: A Machine Learning Approach to Derive Aerosol Properties from All-Sky Camera Imagery, Remote Sensing, 15, https://doi.org/10.3390/rs15061676, 2023.

Schuster, G., Dubovik, O., and Holben, B.: Angstrom exponent and bimodal size distributions, J. Geophys. Res., 111, 1–14, https://doi.org/10.1029/2005JD006328, 2006.

Sinyuk, A., Holben, B. N., Eck, T. F., Giles, D. M., Slutsker, I., Korkin, S., Schafer, J. S., Smirnov, A., Sorokin, M., and Lyapustin, A.: The AERONET Version 3 aerosol retrieval algorithm, associated uncertainties and comparisons to Version 2, Atmospheric Measurement Techniques, 13, 3375–3411, https://doi.org/10.5194/amt-13-3375-2020, 2020.

Snik, F., Rietjens, J. H. H., Apituley, A., Volten, H., Mijling, B., Di Noia, A., Heikamp, S., Heinsbroek, R. C., Hasekamp, O. P., Smit, J. M., Vonk, J., Stam, D. M., van Harten, G., de Boer, J., Keller, C. U., and Scientists, 3187 iSPEX citizen: Mapping atmospheric aerosols with a citizen science network of smartphone spectropolarimeters, Geophysical Research Letters, 41, 7351–7358, https://doi.org/10.1002/2014GL061462, 2014.

Stokes, G. M. and Schwartz, S. E.: The Atmospheric Radiation Measurement (ARM) Program: Programmatic Background and Design of the Cloud and Radiation Test Bed, Bulletin of the American Meteorological Society, 75, 1201–1222, https://doi.org/10.1175/1520-0477(1994)075%3C1201:TARMPP%3E2.0.CO;2, 1994.

Tohsing, K., Schrempf, M., Riechelmann, S., and Seckmeyer, G.: Validation of spectral sky radiance derived from all-sky camera images - A case study, Atmospheric Measurement Techniques, 7, https://doi.org/10.5194/amtd-7-69-2014, 2013.

Valdelomar, P., Gómez-Amo, J. L., Peris-Ferrús, C., Scarlatti, F., and Utrillas, M. P.: Feasibility of Ground-Based Sky-Camera HDR Imagery to Determine Solar Irradiance and Sky Radiance over Different Geometries and Sky Conditions, Remote Sensing, 13, 5157, https://doi.org/10.3390/rs13245157, 2021.

Zhang, Z., Li, J., Dong, Y., Zhang, C., Li, Q., and Gao, L.: Retrieval of global aerosol and surface properties from the Gaofen-5 Directional Polarimetric Camera measurements, Atmospheric Measurement Techniques, 19, 2555–2574, https://doi.org/10.5194/amt-19-2555-2026, 2026.